Real-time thermography system for composite welding: undamaged baseline approach

F.Flora, M.Boccaccio, GPM Fierro, M.Meo

Abstract

The aerospace industry's current focus on recyclable materials and low-cost processes has accelerated research and implementation of thermoplastics matrix composites (TPC). In the last decades, researchers have researched weldability of these materials as a valid alternative to conventional mechanical fastening and adhesives, for improving the strength of the joint. Automatic induction welding of carbon fiber TPCs is one of the most promising techniques due to its numerous benefits, such as elevated energy efficiency and highly localised heat. As for all the manufacturing techniques, the importance of efficiently detecting the presence of defects during TPCs welding has pushed the need for automated *real-time* non-destructive evaluation (NDE) systems. This paper focuses on the development of an efficient NDE technique able to detect the presence of alterations and defects in *real-time* during the welding process. This technique relies on Infrared (IR) active thermography inspections performed using the induction welding heat as the source and an undamaged baseline methodology to detect differences in the heat field. The procedure was experimentally analysed by means of an apparatus capable of automatic welding of samples, performing the *real-time* NDE during the process. Results show the efficiency of the method to localise the damaged area and characterise the defects during the welding. The undamaged baseline methodology was proven to better clarify shape and location of defects, allowing for an efficient detection of damaged samples and areas where more detailed inspections can be performed after the welding process by means of the same IR apparatus.

Keywords: Welding; thermography; thermoplastic

Introduction

Recent interest of industries (such as aerospace and automotive) in new materials like carbon fiber reinforced polymers (CFRPs) has led to the development of advanced automated manufacturing systems. Some examples are automated fiber placement (AFP), automated tape placement (ATP) and automated welding systems [1].

The welding process, also known as fusion bonding, is one of the main advantages in the use of thermoplastic composites (TPCs) materials, where the material temperature is increased above the matrix melting point and joined to other parts. Automated welding processes produce high strength joints, without altering the structural integrity of the parts, as in the case of mechanical fastenings. Da Costa et al. [2] published a review on the welding techniques available for TPCs, differentiated by the heat source: ultrasonic, induction, microwave, resistance, hot plate, IR and laser welding are some of the most

common. Particular interest is growing in research regarding induction welding, which involves the generation of heat by means of eddy currents generated at the welding interface using a high-frequency magnetic field, efficiently producing high quality joints between the composite and other thermoplastic [3,4] or metallic [5,6] materials. However, welded components need to be checked, particularly in critical application where weld failure can be fatal, such as nuclear field, power plants, pressure vessels and load-bearing structural component [7–9]. Indeed, the presence of a damage in the welded area may lead to a strong reduction of the joint strength, and thus a catastrophic premature failure of the final part. Thus, the importance of efficiently detecting the presence of defects during TPCs welding has pushed the need of automated non-destructive evaluation (NDE) systems.

Non-destructive testing (NDT) techniques have been developed over the years in many engineering processes as a powerful tool to reveal presence of damage in materials without affecting the structural and chemical properties of the inspected component. Conventional NDT methods used in industry for damage detection generally include liquid penetrant, magnetic particle, and phased-array ultrasonic testing [10–12]. However, these techniques are based on contact inspections, thus representing a limitation where material contamination with coupling medium or contact sensor is prohibited. Nonlinear air-coupled ultrasound [13], radiography [14], and eddy current testing [15] provide non-contact inspections where coupling liquid are inappropriate, e.g. in such engineering processes where contact technique or immersion may not be practical, or, where water can affect the property of the material being inspected, such as reinforced plastics, electronic-packaging materials, wood, or stainless steel [8,16–19]. However, the above-mentioned technique generally requires voluminous equipment and time-consuming data processing and cannot be implemented in the welding apparatus to have a real-time evaluation of the inspected part. Therefore, there is need of an automatic NDE technique capable of performing damage evaluation of the joint during the welding procedure. Active infrared (IR) thermography techniques are widely used for surface and internal damages in many engineering contexts, in both military and civil engineering [20–22]. An IR-camera is employed to detect any non-uniform heat distribution along the surface of the sample, subjected to heat source or ultrasonic excitation [23,24]. In the case of induction welding of TPCs, *real-time* thermography NDE of the welding line is a possible solution for detection of damages in the part, but it is limited by the heterogeneity and intensity of the heat field. In addition, most of the defects, such as delamination at welding interface, are parallel to the eddy current field, thus not creating a significant interference in the heat generation [25,26]. Indeed, induction heating of CFRPs is based on the flow of an electric current through closed carbon fiber loops. Given that the density of closed loops of carbon fibers may substantially vary through the thickness of the part, CFRP is a highly inhomogeneous conductive material when compared with metals [27].

Many studies about eddy current testing (ECT) can be found in literature, which is a damage localisation technique based on detecting alterations in eddy currents induced in the part. De Goeje *et al.* [26] studied the influence of fiber orientations and process parameters on the ECT in creating C-scan images,

highlighting its limitations and differences between unidirectional and weave reinforcements. Koyama et al. [27] illustrated some of the problems relating to the use of ECT for CFRPs, proposing some inspecting probes able to efficiently detect the damages in the part. A strong limitation of these probes relies on the optimisation needed to be designed in function of part and material. He et al. [28] investigated the use of eddy current pulsed thermography for NDE of impacted CFRP using probs in reflection and transmission modes, obtaining the best results with the last. Heuer et al. [29] provided a detailed study on the efficiency of high frequency ECT system in detection of different material properties and defects, with the possibility of integrating the NDT system into some manufacturing processes for thermoset composites. Another example of integrated ECT system is the one proposed by Fierro et al. [30], where a thermography induction NDT system was used during automated fibre placement (AFP) process while principal component analysis (PCA) of the raw thermal images was conducted, obtaining clear images of typical damages. In a previous work, Flora et al. [31] provided an experimental study about a *real-time* thermography system during induction welding, which was able to detect damage in samples, but required further NDE analysis for the complete characterisation of the defects due to the inhomogeneities in the heat field.

Generally, the system and its parameters used for ECT NDE thermography of composite materials need to be customised for the specific part in order to overcome the natural inhomogeneities in the heat field and detect the real defects. This optimisation becomes more complicated when NDE is needed *in-situ* and *real-time* during automated induction processes, such as induction welding. Indeed, the parameters used for the welding process, such as frequency, movement speed, coil shape and position, may be far for the ones optimised for the NDE.

This work is focused on the development of a technique aimed to solve these limitations, easing the implementation of NDE thermography system to a general automated induction process. The technique is based on the building of an undamaged baseline that, coupled with the repeatability of the automated process and parameters, allows for the building of a thermographic image of the part and efficiently detect large and small variations in the heat field. Indeed, automated induction welding machines designed for large-scale productions can weld with a rate up to 150 parts per minute [32]. Based on this it is possible to timely identify damaged parts and alterations in the system components, allowing for a prompt adjustment of the manufacturing line and reduction of the rejected parts, leading to large cost saving. The proposed system is able to detect discrepancies in the process automatically, highlight the defected part and perform a local *post-welding* thermography scan in an automatic manner, without the intervention of the manual operator. In order to experimentally prove the efficiency of the technique, the NDE thermography system is combined with an automated induction welding process composed of an induction coil and a pressure roller connected to a gantry system. Samples were welded using Titanium and TPCs parts, and some of the typical defects for this kind of process were simulated between the parts. Thermal data was recorded during the process using IR cameras and an algorithm was used to automatically allocate them in time and space, leading to a 3D thermal data matrix. Thermal images were obtained by

characterising the thermal intensities (T_I) in three different features (depth, width, aggregate integrations) and subtracting the undamaged baseline, which was built scanning three undamaged samples. Results show the improvements provided using the undamaged baseline in the defect localisation, sizing and clarity when compared to traditional thermography-based analysis.

Induction heating

Induction heating is a well-established method for generation of heat in magnetically susceptible and electrically conductive material. Applying an alternate current to a coil made of a conductive material (induction coil), a time variable magnetic field with the same frequency is generated in the area around it. When the conductive part is placed into this primary magnetic field, eddy currents are generated through the material, which themselves generate heat, meanly due to Joule losses, and a secondary magnetic field. This phenomenon, illustrated in Figure 1, can be used for NDE of the parts by means of thermographic image analysis or using probes, usually a secondary coil, able to detect the properties of the secondary magnetic field, and thus identifying eventual alterations. In addition, the generated heat can be used to melt the part and weld it to other materials, such as in the case of induction welding of TCPs.

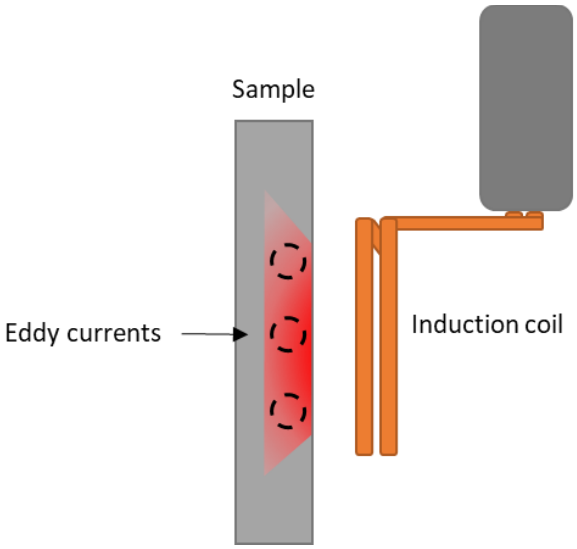

Figure 1 - Induction heating process

Eddy currents need closed-loop of conductive material in order to be generated. This is easy for a homogeneous conductive material, such as metals, where every section of the part is itself a closed-loop. Indeed, induction heating and welding was originally widely used for metals [33]. Only in the last decades this technique was extended to other materials such as CFRPs, with thermosetting or thermoplastic matrix, where the carbon fiber reinforcement plays the role of the magnetically susceptible and electrically conductive component. Given the heterogeneity of composite materials, the presence of carbon fiber closed-loops is not always guaranteed. An example is the unidirectional laminate, where all the reinforcement is aligned in one direction, thus not creating enough contacts to generate a significant quantity of eddy currents [34]. For induction welding, in

the cases where the parts themselves cannot be heated by generation of eddy currents, heating elements sensible to the magnetic field are inserted at the welding interfaces in order to generate the heat [35].

When the part is immersed in the magnetic field generated by the coil, the eddy currents tend to flow along the surface rather than through the depth and dissipates quickly. This so-called "skin effect" is usually measured with the standard depth of penetration δ, that is the point in depth were eddy current field is decreased by the quantity $1/e$ (approximately 37%) [36]. This quantity is a function of the current frequency f and the electrical conductivity σ, and magnetic permeability μ of the material as given by the following equation.

$$\delta = \sqrt{\frac{1}{\pi\sigma\mu f}} \qquad (1)$$

The frequency of the eddy currents is the same as the alternating current induced in the induction coil. Therefore, the eddy current field increases with the frequency following the Faraday's law of induction states [29]. For materials with low electrical conductivity, such as CFRPs, high frequencies are needed to generate a significant amount of eddy currents and, thus, of heat. Despite the high values of frequency (f), the value of δ is maintained relatively high enough thanks to the low electrical conductivity (σ) of the material, generating eddy currents in depth.

The heated sample acts as an ohmic resistor, therefore the induced current, and thus the heat, is proportional to the generated power, defined by the following formula [34]:

$$P = \frac{(2\pi f \mu H A)^2}{R} \qquad (2)$$

where H the magnetic field intensity, A the sectional area and R the resistance of the conductive material. From equations (1) and (2), the intensity and depth of the heat, for both welding or NDE purposes, is a function of several factors: frequency of the magnetic field, coil geometry and distance, sample dimensions and material properties. The optimisation and design of the induction system is complicated due to the non-linear relation between these parameters and is therefore unique for each application, making the combination of manufacturing and NDE processes a challenge.

Thermal data analysis

Infrared (IR) active thermography is a NDE technique widely used for damage detection in structures and materials in many sectors, such as aerospace, civil engineering and military [20,22,24,37]. IR techniques generally require an external energy source to induce a gradient of temperature within damaged and undamaged areas in the inspected component. As regards induction heating, damage detection relies on the change in the distribution of locally induced eddy currents due to damage region, thus leading to a higher heat generation near the cracks [38,39].

In this context, heat diffusion trough a solid represent a three-dimensional problem which can be modelled by Fourier's heat equation [40]:

$$\nabla^2 T = \frac{1}{\alpha}\frac{\partial T}{\partial t} \qquad (3)$$

Where T and t denote the temperature and time variables, respectively, $\alpha = k/\rho c_p$ is the thermal diffusivity of the inspected material, k is the thermal conductivity, ρ and c_p represent the density and the specific heat at constant pressure, respectively. A one-dimensional solution of equation (3) in a semi-infinite isotropic and homogeneous solid can be evaluated for the propagation of a Dirac heat pulse, which represents an ideal waveform defined as an instantaneous and intense unite-area pulse. The solution is given by:

$$T_i(z,t) = T_i(z,t=0) + \frac{Q}{\sqrt{kc_p\rho\pi t}} e^{\left(-\frac{z^2}{4\alpha t}\right)} \qquad (4)$$

Where Q is the energy absorbed by the surface and z is the space variable through the sample thickness. A Dirac heat consists of periodic wave containing all the frequencies and amplitudes, and such a waveform cannot be reproduced. In practice, a heat pulse generated by a photographic flash or an induction coil has approximately a square shape. With this regard, the signal is a periodic wave with several frequency harmonic components, depending on the pulse duration. Indeed, the shorter the pulse, the broader the frequency range. At the surface (i.e. z = 0), equation (4) can be written as follows:

$$T_i(z=0,t) = T_i(z,t=0) + \frac{Q}{\sqrt{kc_p\rho\pi t}} \qquad (5)$$

Although equation (6) only represents an approximated solution of the complex 3-D Fourier's law in equation (3), several pulsed thermography-based processing techniques rely on this simplification to perform quantitative and qualitative analysis [41–43]. The second term of equation (5) quantifies in-time thermal distribution across the sample, which can be used to conduct NDE thermography investigations.

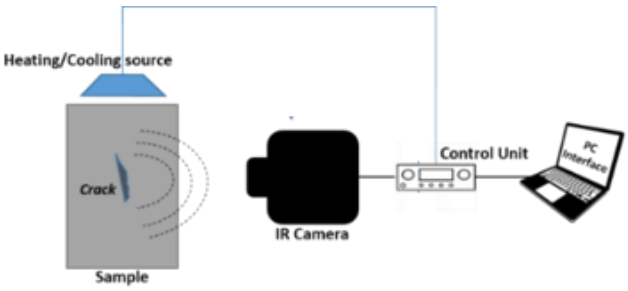

Figure 2 - Infrared active thermography general setup

Data acquisition and experimental setup of a general NDE thermography procedure are shown in Figure 2. The sample is subjected to a heat source, which

in this work is Joule losses due to the eddy current generated by the induction coil. The heat field reflects the shape of the induction coil, which is of hair pin type, and is also influenced by the conductive properties of the material. As time elapses, the thermal front travels within the sample, and the superficial temperature will decrease nearly uniformly. Contrarily, subsurface inhomogeneities behave as a resistance to heat flow which produces anomalous temperature distributions at the surface.

In this work, during the process, IR cameras move with the welding system, recording images (frames) of a part of the heated sample, each of them representing the thermal status of a specific area and time. Thermal data were analysed in a similar manner highlighted in previous works [30,31]. Knowing the position along the welding line and recorded time of each frame, it was possible to build the structure of the thermal data in space and time.

Indeed, given that a frame is a M x N matrix of pixels, and thus thermal data, of the sample, it is possible to overlap the images aligning the pixels relative to the same point in space at different times. The image relative to the part of the sample that was not recorded by the cameras at each time were filled with zeros, obtaining M x N' matrixes of thermal data of the sample. Figure 3 illustrates the recording of the thermal images during the welding process at three different points in time.

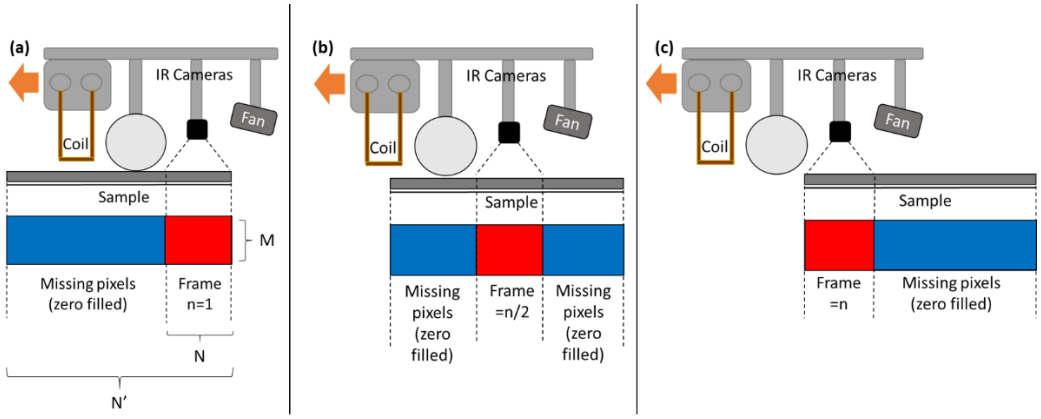

Figure 3 - Thermal images capturing process at the beginning (a), middle (b) and end (c) of the welding line.

$$dT_I(x,y) = \sum_{t=1}^{n} T_I(x,y,t) \qquad (6)$$

Stacking all the frames, which total number n depends on the moving velocity of the system and the frame rate of the cameras, a 3D matrix of thermal data is obtained, where the third dimension represents the number of frames, and thus the time t. The other two dimensions of the thermal intensity T_I 3D matrix represents the two directions of each frame, labelled here as x and y, and can vary from 0 to N' and M, respectively. Summing the values in the T_I 3D matrix along the time, one obtains a final thermal image (dT_I 2D matrix) of the sample, as described by equation (6). The building of the thermal data matrix and final image is illustrated in Figure 4.

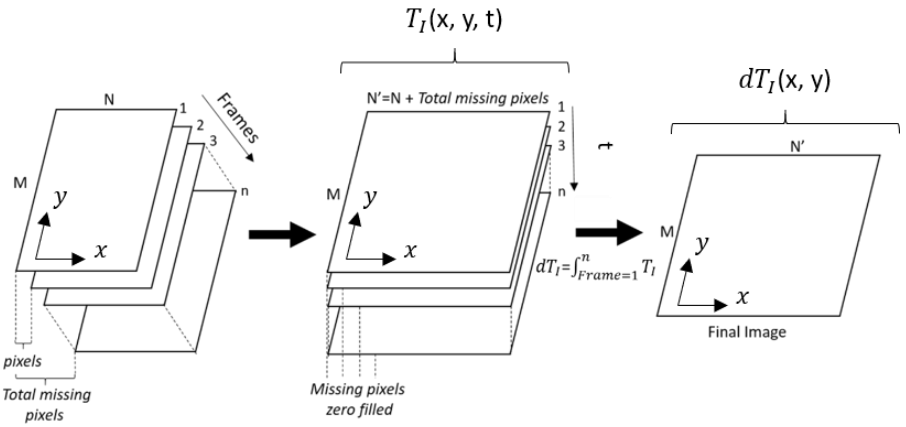

Figure 4 - Summary of thermal image processing and building of T_I 3D matrix and dT_I image.

$$wT_I(x,t) = \sum_{y=1}^{M} T_I(x,y,t) \qquad (7)$$

$$aT_I(x) = \sum_{t=1}^{n} wT_I(x,t) \qquad (8)$$

The high repeatability of the welding process allows for further simplification of the process used for analysis of the thermal images illustrated in Figure 4. Figure 5 illustrates the calculation process applied to obtain width [wT_I, (b)] and aggregate T_I [aT_I, (c)] images. The term wT_I was calculated by summing over the width y of the frame stack, as described in equation (7), providing a final image of the T_I through the depth t and length x of the sample. The aT_I provides a single line plot of the aggregate intensity values by integrating over the number of frames t of wT_I, as described in equation (8).

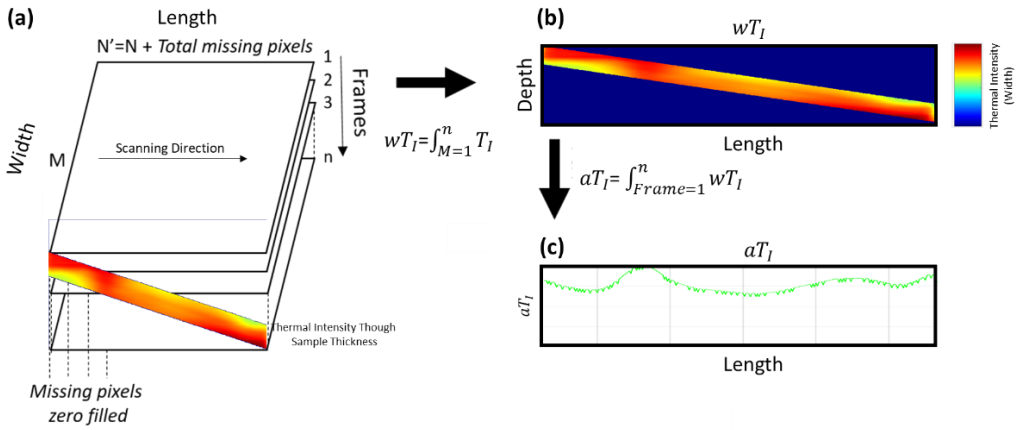

Figure 5 - Processing of thermal images using the frame stack (a), thermal intensity over the width (b) and the final aggregate thermal intensity (c)

Induction welding of TPCs is characterised by high repeatability for a given set of samples. The technique proposed in this work relies on the process repeatability, aiming to detect any kind of alteration in the heating field. With this

regard, the baseline was built by welding and testing a set of undamaged samples. The undamaged results in terms of dT_I, wT_I and aT_I values were subtracted from the ones obtained from tested samples, thus highlighting any variation in the heat field during the welding, as illustrated by the following equations:

$$dT_{I_{sub}} = dT_I - dT_{I_{undamaged}} \quad (9)$$

$$wT_{I_{sub}} = wT_I - wT_{I_{undamaged}} \quad (10)$$

$$aT_{I_{sub}} = aT_I - aT_{I_{undamaged}} \quad (11)$$

Experimental setup

In order to simulate the automatic induction welding process, the same system showed in [31] and illustrated in Figure 6 was used. The system, consisting of an induction coil, compression roller, IR cameras and a cooling fan attached to a gantry system, is able to pass over the samples and in order heat up, compress and cool down the two welding parts. The velocity used for the system and all its components is 6 mm/min. The induction heating system consists in an Ambrell® EasyHeat Induction Heating System 0224, with a maximum power of 2.4 kW and frequency in the range of 150-400kHz. The induction coil is made of a copper tube with 8 mm outside diameter and is of pin type shape, with a length of 150 mm and an internal distance of 10 mm (see number 1 in Figure 6). The pressure was applied using 50 mm diameter PTFE roller attached to two steel springs of a known elastic spring constant. The applied force was controlled during the process by measuring springs displacement and adjusting the pre-compression nuts. To record the thermal data during the process, two IR cameras (FLIR Lepton 3.12 µm, array format 160x120 pixels, frame rate 8.7 Hz, thermal sensitivity <50 mK) were used for the *real-time* scanning of the samples after the compression, for a total of 280 frames recorder for each sample. A fan was attached pointed towards the area after the compression in order to provide a fast cooling down of the samples, that gives benefits for both the welding process and the NDE analysis. Indeed, after the compression and welding of the part, the thermoplastic matrix needs to return below the crystallization temperature to avoid decompaction and delamination. On the other side, according to equation (3), the introduction of a cooling step after heating/welding increases the instantaneous temperature gradient (i.e. $\partial T/\partial t$), thus enhancing thermal imaging resolution [44].

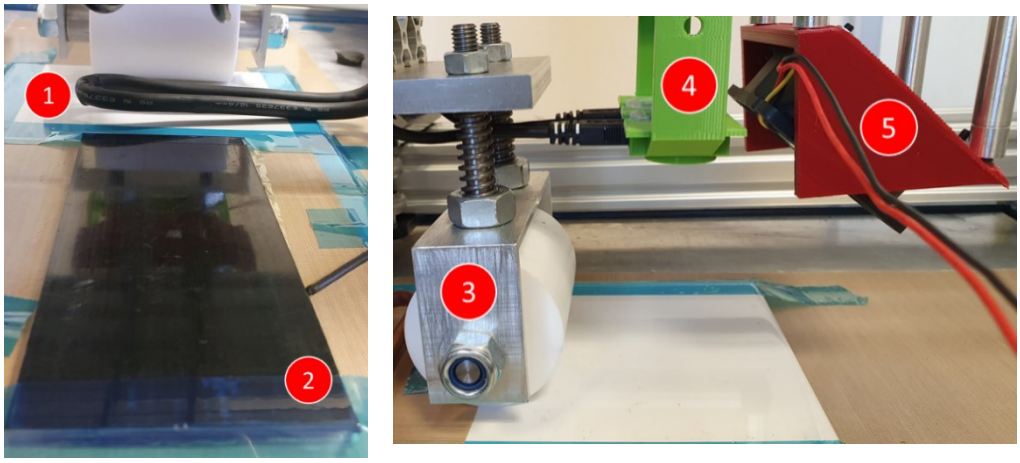

Figure 6 - Welding system: induction heating coil (1); PA6-Ti sample (2); PTFE pressure roller (3); rear IR cameras (4); cooling fan (5) [30]

The welding tests were performed between TPCs and Titanium samples. In order to have a comparison with similar tests performed without the undamaged baseline, samples with the same layout as the ones used in a previous work [31] were used: 150x65 mm samples manufactured using SGL Carbon® UD carbon fiber-reinforced PA6 laminates (2 mm thickness) and Ti 15-3-3-3 foils (0.1 mm thickness). The induction field was generated using a current of 151.2 A and a frequency of 290 kHz, while a force of 60 N was applied to the samples. The welding parameters were selected during a preliminary experimental campaign in order to provide the right temperature and pressure at the interface between the titanium foil and the TPC sample, without overheating and damage the material. In order to prove the reliability of the system for damage detection, four samples were tested, outlined in Table 1 and Figure 7. The first sample is an undamaged sample; therefore, the results are expected to show the absence of defects. The other three sample present different kind of defects: foam and titanium inserts with different dimensions, a hole and a wrinkle in the titanium foil. In the last sample, different damages were added in sequence to make the characterisation more complicated. Indeed, every damage creates alteration in the eddy currents that could lead in a strongly deformed heat field, hiding the presence of more than one defect.

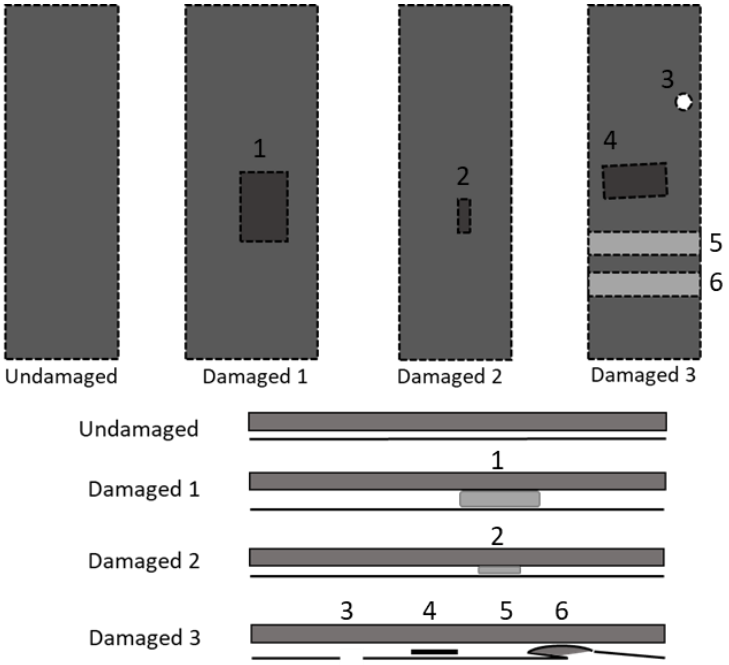

Figure 7 – Samples damage configuration [31]

Table 1 - Samples nomenclature and damage dimensions

Sample	*Damage*		*Dimensions*	*Label*
Undamaged (UD2)	Undamaged		-	
Damaged 1 (D1)	Foam patch		10x20x10 mm	1
Damaged 2 (D2)	Foam patch		10x10x3 mm	2
Damaged 3 (D3)	Hole		5 mm diameter	3
	Ti patch		20x30x0.1 mm	4
	Wrinkle	Air gap	10x65 mm	5
		Overlap	10x65 mm	6

During the tests, the system recorded and analysed the thermal data in *real-time* using the algorithm previously described. If an alteration is detected, the sample can be recognised as damaged by the system analysing the difference from the undamaged results and flagging values over a defined threshold, in particular for the aT_I profiles. In function of the dimensions of the sample, and therefore the amount of data to be analysed, and the computational capabilities of the computer, the analysis can take from just a few seconds up to some minutes. In the case of the samples and system used in this work, the analysis took around 45 seconds for each sample.

Results and discussion

The first tests were performed on three undamaged samples in order to build the undamaged baseline (UD). The integrity of the samples was double checked by using ultrasonic C-Scan, in order to verify the absence of unexpected defects

such as delamination. In order to prove that the subtraction method recognised the absence of defects, an additional undamaged sample (UD2) was inspected. Thermal images were recorded and evaluated during the process.

Figure 8a and Figure 8b show dT_I images for the baseline and the undamaged samples respectively. As shown in Figure 8, the heating field is not uniform in both cases, especially between the central area and the edges, but the heating hotspots and patterns between the two images clearly match. After subtraction, variability between the values of dT_I was very low, as expected. The subtracted values of dT_I allows the building of a final thermal image (Figure 8c) that clearly shows the absence of alterations in the heat field.

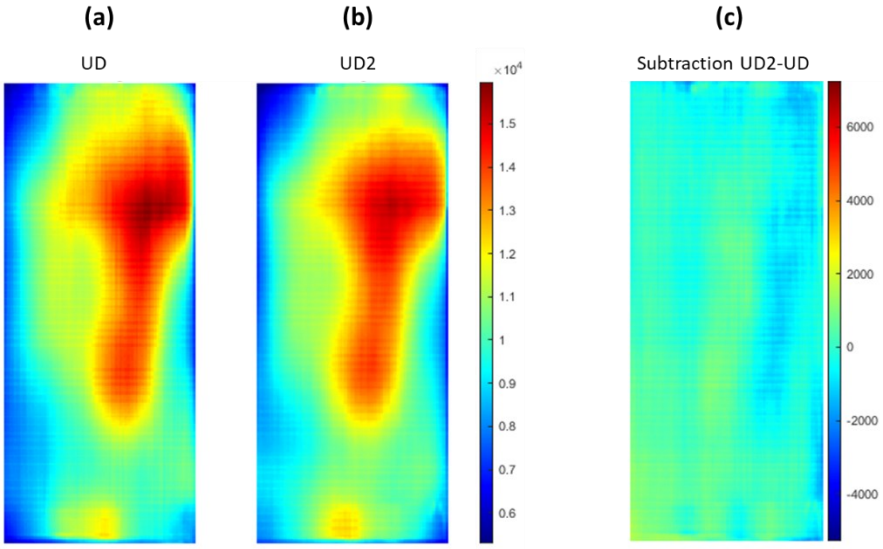

Figure 8- Thermal dT_I images for undamaged baseline (a), undamaged sample (b), baseline subtraction $dT_{I_{sub}}$ (c).

Figure 9 shows the wT_I (a-b) and aT_I (c-d) responses for the baseline and the undamaged sample, with the direct comparison highlighted in (e). The abscissa in the graphs corresponds to the sequential number of the recorded frame, and therefore the position along the sample length. There are marginal differences between the two undamaged cases (UD and UD2), and the subtracted aT_I line plot results in an almost flat response. This indicates that there is no significant difference between the welding and material integrity of these two samples. The propagation of thermal waves across discontinuities (defects) results in varied heat field of inspected samples in that region. This variation should be clear when compared with a baseline (defect-free) measurement, with the results highlighted in the following sections.

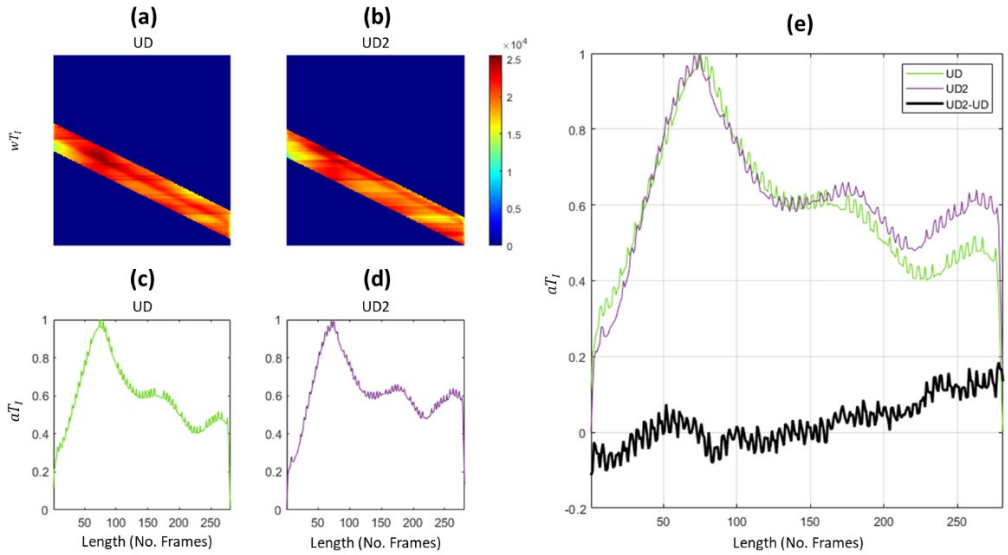

Figure 9 - wT_I for UD1 (a), wT_I for UD2 (b), aT_I for UD1 (c), aT_I for UD2 (d), $aT_{I_{sub}}$(e).

Following the same procedure and parameters used for the undamaged samples, D1 damaged sample was welded, *real-time* recording thermal data from the welding line. The resulting thermal dT_I image of the sample D1 is shown in Figure 10b, where an irregularity in the heat distribution is already visible. Defect location and shape become clearer when the subtraction of the undamaged baseline (a) is applied, obtaining the image in Figure 10c

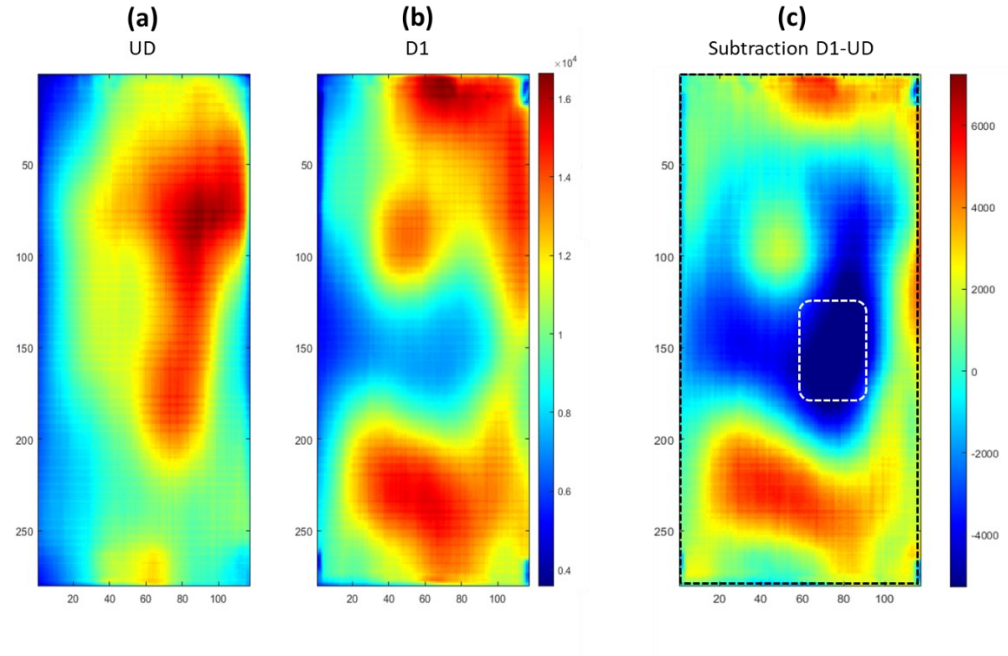

Figure 10 - Thermal dT_I images for undamaged baseline (a), damaged sample D1 (b), baseline subtraction $dT_{I_{sub}}$ (c).

Figure 11 shows the wT_I (a-b) and aT_I (c-d) calculations for the baseline and damaged samples. The comparison and subtraction of the two aT_I line plots (e) identify the location of the damage along the sample, highlighted in the plot. A visual representation of the sample and damage was added at the bottom part of the plot to show the accuracy of the technique. The results in both Figure 10 and Figure 11 show an accumulation of heat towards the top and bottom of the

D1 sample. This is probably due to the fact that the heat generated in the titanium foil is shielded by the large foam, accumulating in the area before and after the damage.

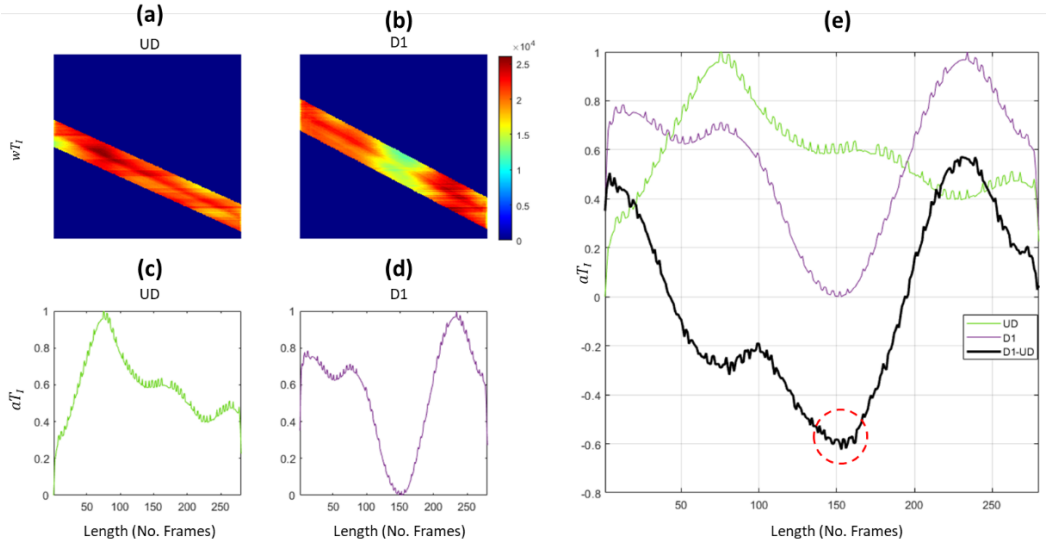

Figure 11 - wT_I undamaged baseline (a), wT_I image for D1 (b), aT_I undamaged baseline (c), aT_I profile for D1 (d), $aT_{I_{sub}}$ (e).

Figure 12 shows thermal images from the welding of sample D2, which present the same kind of defect of the D1 sample but of a considerably smaller size. As shown in dT_I image of the D2 sample (b), damage affects heat profile at different points. In Figure 12c related to the subtraction image, damage creates a colder area in the centre of the sample, dissipating the heat and thus creating hot spots in the area around it.

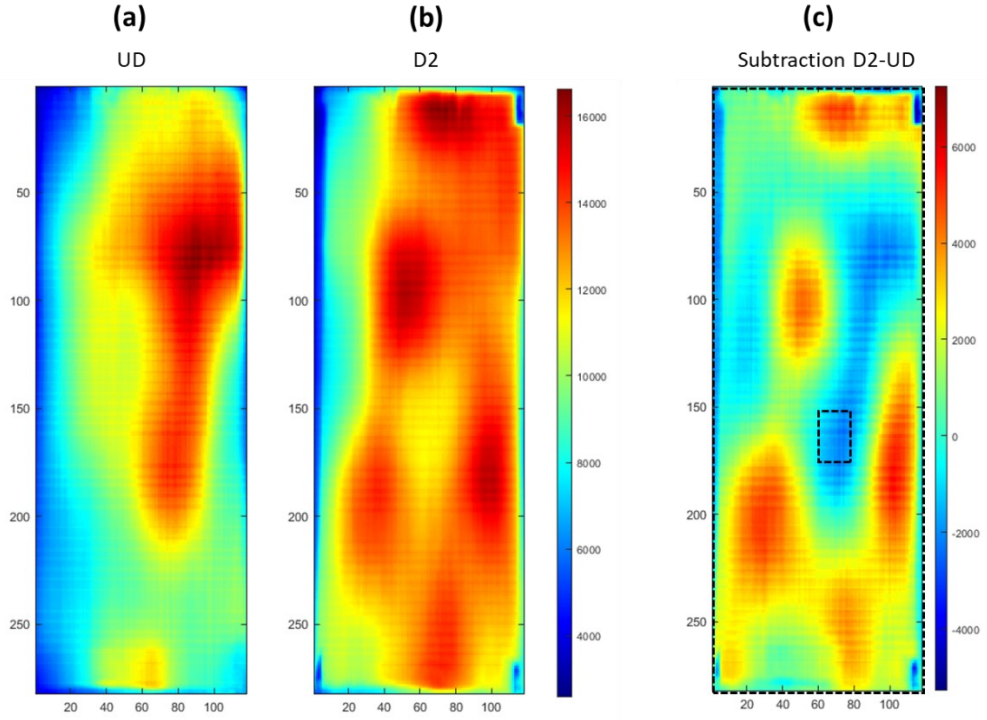

Figure 12 - Thermal dT_I images for undamaged baseline (a), damaged sample D2 (b), baseline subtraction $dT_{I_{sub}}$ (c).

Figure 13 shows the wT_I (a-b) and aT_I (c-d) responses for both UD baseline and D2 sample. The difference between the two aT_I curves, highlighted in the plot (e), is far from being flat, thus indicating presence of defects. The damage location corresponds to the non-zero values highlighted (1) in the curve. In addition, a second peak (2) was detected, thus suggesting the presence of a second damaged area. This area was successively linked to an unwelded part of the sample by visual inspection of the welded area. In this second sample, the damage is difficult to be distinguished, due to the smaller size of the defect and the generation of numerous secondary alterations in the heat field and the second unexpected defect (unwelded zone). However, from the analysis of the difference with the UD results, it is possible to determine the presence of defects in the sample, thus flagging it as damaged, which is the main aim of the technique.

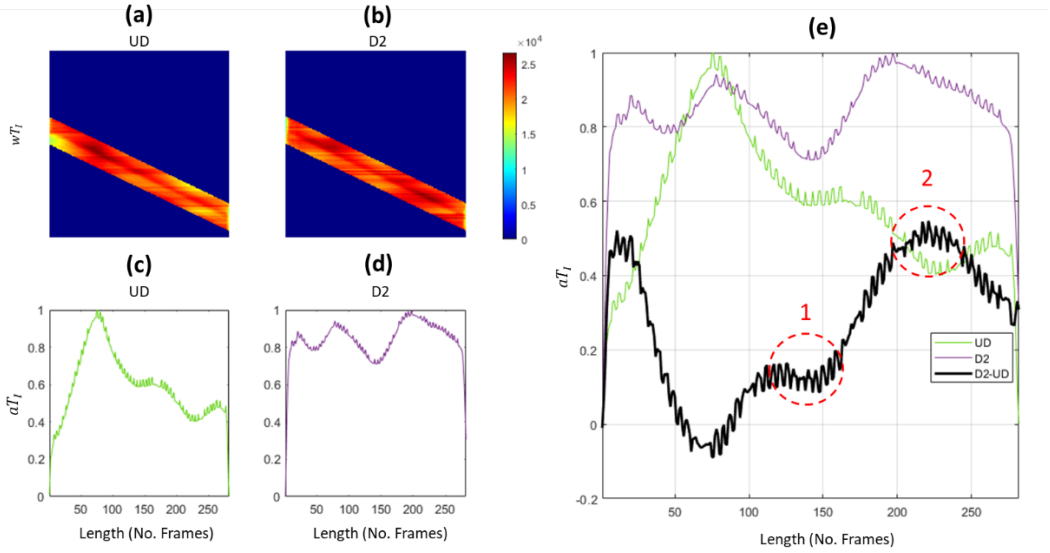

Figure 13 - wT_I undamaged baseline (a), wT_I image for D2 (b), aT_I undamaged baseline (c), aT_I profile for D2 (d), $aT_{I_{sub}}$ (e).

As described in the previous section, sample D3 presents three defects: a hole in the top part of the Ti foil, a titanium patch and a foil wrinkle. The scope of inspecting multiple defects in the sample is to test the efficiency of the undamaged baseline technique in the detection of more complex and overlapping discontinuities in the heat field. Figure 14 shows the dT_I images of the undamaged baseline (a), D3 sample (b) and the dT_I subtraction image (c). As shown in the subtraction image, the heat profile of the sample presents many alterations in correspondence with the defects. In central part, the presence of the titanium insert is clearly located by the hot spot (1). In the bottom part of the samples, two horizontal alterations are detected: a cold area (2) which correspond to an air gap before the wrinkle, followed by a hotter area (3) due to the higher amount of metal material at the wrinkle. Finally, in the top part of the welding area, a cold spot is clearly detected in correspondence with the hole (4).

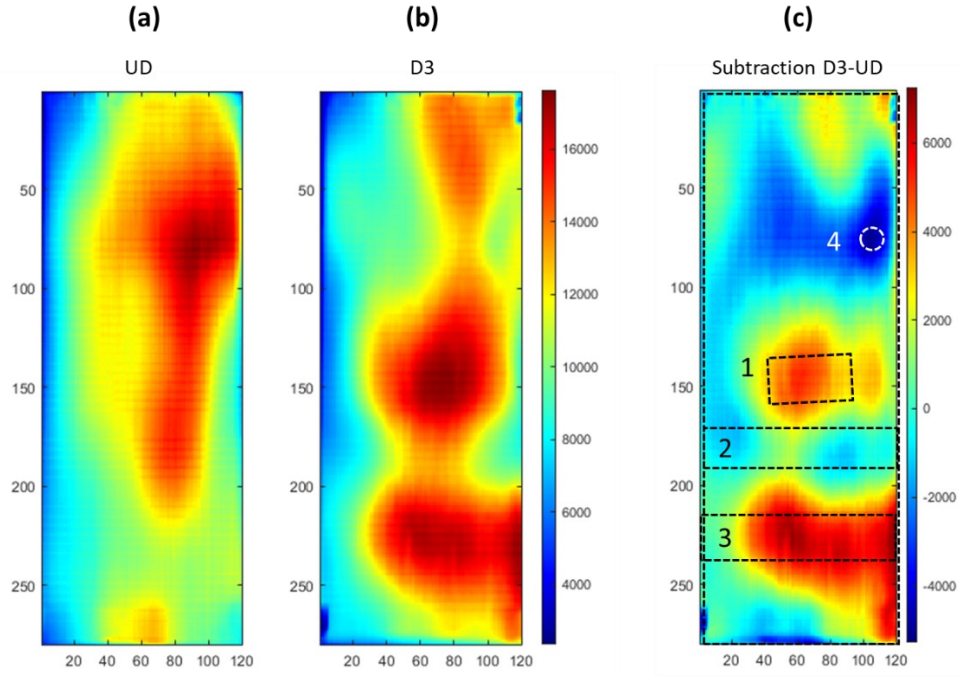

Figure 14 - Thermal dT_I images for undamaged baseline (a), damaged sample D3 (b), baseline subtraction D3-UD (c).

Figure 15 shows the wT_I (a-b) and aT_I (c-d) for both undamaged and damaged samples. A good estimation of defects location can be identified by plotting the difference between the two total temperature profiles (e). As highlighted in the plot, each peak of the subtracted curve corresponds to the position of a defect. In the case of the wrinkle, there are a positive and negative peak arises, as expected.

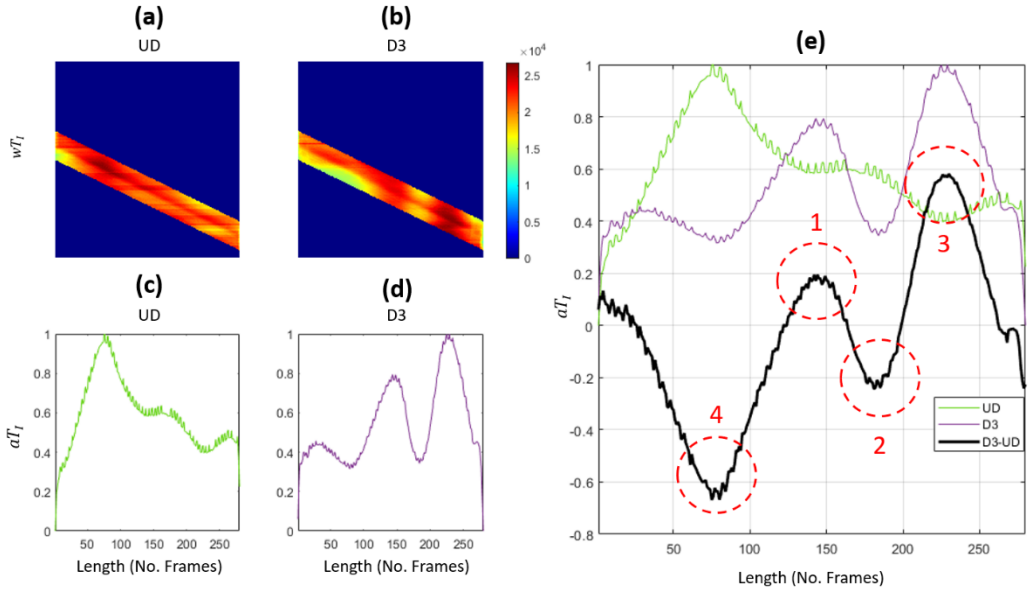

Figure 15 - wT_I undamaged baseline (a), wT_I image for D3 (b), aT_I undamaged baseline (c), aT_I profile for D3 (d), $aT_{I_{sub}}$ (e).

In Figure 16 the aT_I and $aT_{I_{sub}}$ profiles are summarised for all the tested samples with illustrations of the samples and defects. As it is possible to see, every defected sample showed a non-flat subtraction curve. The aT_I result with

undamaged baseline subtraction is a valid method for detection of damaged samples. The process can be easily automated for detecting the eventual presence of peaks during the welding process, highlighting the damaged samples. In order to do this, a damage threshold needs to be defined, thus flagging as damaged every sample that shows values over the limit.

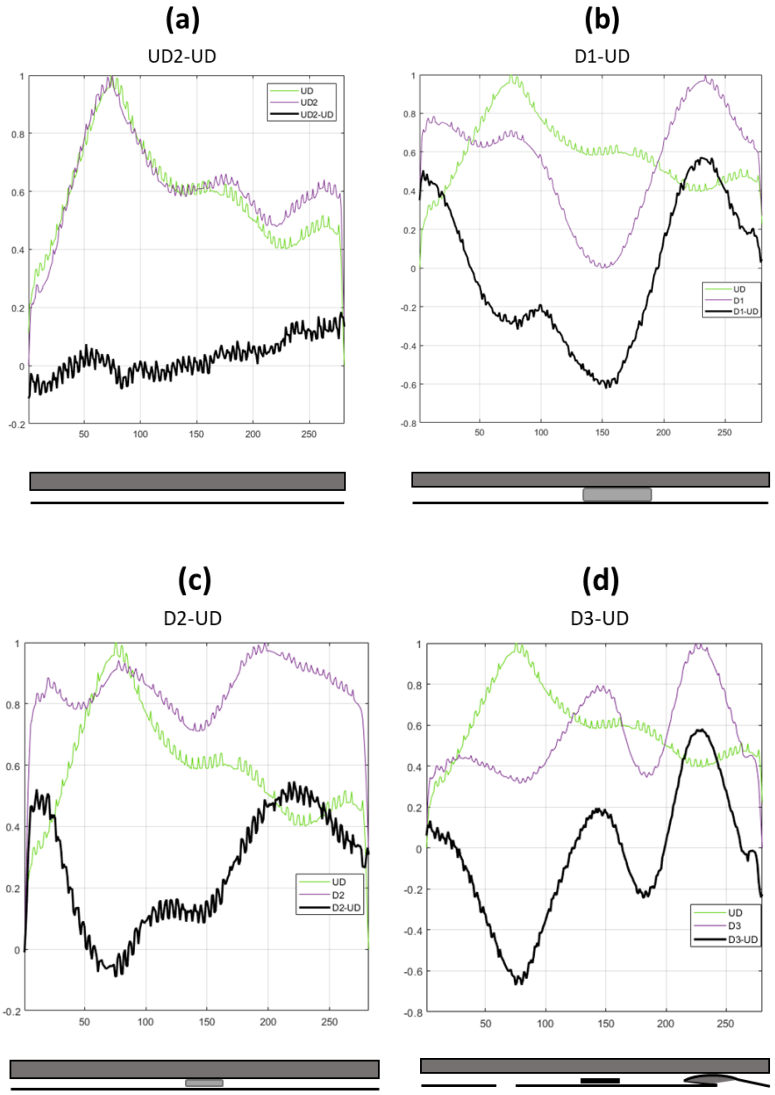

Figure 16 - $dT_{I_{sub}}$ profiles for UD2 (a), D1 (b), D2 (c) and D3 (d) samples with samples illustration

Conclusions

A thermography-based technique for *real-time* non-destructive evaluation of defects during automated manufacturing processes was developed. The technique was tested during electromagnetic induction welding of TPCs to evaluate and characterise various defects. The automated welding process was simulated attaching an induction coil, a pressure roller and IR cameras to a gantry system. Given the high repeatability of the process, thermal images were processed by means of an undamaged baseline methodology. The integral of the thermal response dT_I was calculated for each point of the samples and subtracted from the undamaged baseline in order to highlight the alteration in heat field due to the presence of the defects. In addition, the width (wT_I) and aggregate T_I, (aT_I)

were calculated for each sample. Applying the undamaged baseline subtraction to the aT_I line of the damaged samples, the resulting single line plot peaks were proved to highlight the position of strong alterations, and thus possible defects, in the heat field. Results show the efficiency of the method in *real-time* non-destructive localisation and characterisation of defects during induction welding of TPCs.

Generally, the undamaged baseline technique is able to highlight the heat variation due to the defects although the heat source itself is not homogeneous along the sample. Therefore, the proposed NDE technique can also be applied to other kinds of heat-based manufacturing process with high repeatability.

Acknowledgments: The present work is performed within NHYTE project (NHYTE, 2017–2020). The NHYTE project has received funding from the European Union's Horizon 2020 research and innovation programme under grant agreement No. 723309.

References

[1] Breuer UP. Manufacturing Technology. Commer. Aircr. Compos. Technol., Springer; 2016, p. 73–132.

[2] da Costa AP, Botelho EC, Costa ML, Narita NE, Tarpani JR. A review of welding technologies for thermoplastic composites in aerospace applications. J Aerosp Technol Manag 2012;4:255–65. https://doi.org/10.5028/jatm.2012.04033912.

[3] Pappadà S, Salomi A, Montanaro J, Passaro A, Caruso A, Maffezzoli A. Fabrication of a thermoplastic matrix composite stiffened panel by induction welding. Aerosp Sci Technol 2015;43:314–20. https://doi.org/10.1016/j.ast.2015.03.013.

[4] Stokes VK. Experiments on the Induction Welding of Thermoplastics. Polym Eng Sci 2003;43:1523–41. https://doi.org/10.1002/pen.10129.

[5] Reyes G, Kang H. Mechanical behavior of lightweight thermoplastic fiber-metal laminates. J Mater Process Technol 2007;186:284–90. https://doi.org/10.1016/j.jmatprotec.2006.12.050.

[6] Antico FC, Zavattieri PD, Hector LG, Mance A, Rodgers WR, Okonski DA. Adhesion of nickeltitanium shape memory alloy wires to thermoplastic materials: Theory and experiments. Smart Mater Struct 2012;21:035022. https://doi.org/10.1088/0964-1726/21/3/035022.

[7] Degrieck J, De Waele W, Verleysen P. Monitoring of fibre reinforced composites with embedded optical fibre Bragg sensors, with application to filament wound pressure vessels. NDT E Int 2001;34:289–96. https://doi.org/10.1016/S0963-8695(00)00069-4.

[8] Boccaccio M, Malfense Fierro GP, Meo M, Bolton G. Development and focusing enhancement of nonlinear air-coupled acoustic technique for damage characterization in materials. Mater Today Proc 2020. https://doi.org/10.1016/j.matpr.2020.03.335.

[9] Sheiretov Y, Grundy D, Zilberstein V, Goldfine N, Maley S. MWM-Array Sensors for In Situ Monitoring of High-Temperature Components in Power Plants. IEEE Sens J 2009;9:1527–36. https://doi.org/10.1109/JSEN.2009.2019335.

[10] Zolfaghari A, Kolahan F. Reliability and sensitivity of visible liquid penetrant NDT for inspection of welded components. Mater Test 2017;59:290–4. https://doi.org/10.3139/120.111000.
[11] Pendry J, Smith D, Schurig D. Electromagnetic cloaking method 2017.
[12] Habermehl J, Lamarre A. Ultrasonic Phased Array tools for composite inspection during maintenance and manufacturing. 2008.
[13] Boccaccio M, Malfense Fierro GP, Meo M, Bolton G. Design of passive acoustic hyperbolic-shaped filter for nonlinear ultrasonic inspection method optimization. In: Gath K, Meyendorf NG, editors. Smart Struct. NDE Ind. 4.0, Smart Cities, Energy Syst., vol. 11382, SPIE-Intl Soc Optical Eng; 2020, p. 5. https://doi.org/10.1117/12.2558528.
[14] Shevchik S, Le-Quang T, Meylan B, Vakili Farahani F, Olbinado MP, Rack A, et al. Supervised deep learning for real-time quality monitoring of laser welding with X-ray radiographic guidance. Sci RepoRtS | 2020:10. https://doi.org/10.1038/s41598-020-60294-x.
[15] Sophian A, Tian GY, Taylor D, Rudlin J. Electromagnetic and eddy current NDT: a review. Insight 2001;43:302–6.
[16] Hillger W, Ilse D, the LB-P of, 2012 undefined. Practical applications of air-coupled ultrasonic technique. PdfsSemanticscholarOrg n.d.
[17] Gan TH, Hutchins DA, Billson DR, Schindel DW. The use of broadband acoustic transducers and pulse-compression techniques for air-coupled ultrasonic imaging. Ultrasonics 2001;39:181–94. https://doi.org/10.1016/S0041-624X(00)00059-7.
[18] Wright WMD, Hutchins DA. Air-coupled ultrasonic testing of metals using broadband pulses in through-transmission. Ultrasonics 1999;37:19–22. https://doi.org/10.1016/S0041-624X(98)00034-1.
[19] Blomme E, Bulcaen D, Cool T, Declercq F, Lust P. Air-coupled ultrasonic assessment of wood veneer. Ultrasonics 2010;50:180–7. https://doi.org/10.1016/j.ultras.2009.08.004.
[20] Maldague XPV. Introduction to NDT by active infrared thermography. Mater Eval 2002;60:1060–73.
[21] Dionysopoulos D, Fierro GPM, Meo M, Ciampa F. Imaging of barely visible impact damage on a composite panel using nonlinear wave modulation thermography. NDT E Int 2018;95:9–16. https://doi.org/10.1016/j.ndteint.2018.01.005.
[22] Hung YY, Chen YS, Ng SP, Liu L, Huang YH, Luk BL, et al. Review and comparison of shearography and active thermography for nondestructive evaluation. Mater Sci Eng R Reports 2009;64:73–112. https://doi.org/10.1016/j.mser.2008.11.001.
[23] Fierro GPM, Calla D, Ginzburg D, Ciampa F, Meo M. Nonlinear ultrasonic stimulated thermography for damage assessment in isotropic fatigued structures. J Sound Vib 2017;404:102–15. https://doi.org/10.1016/j.jsv.2017.05.041.
[24] Madruga FJ, González DA, Mirapeix JM, López Higuera JM. Application of infrared thermography to the fabrication process of nuclear fuel containers. NDT E Int 2005;38:397–401. https://doi.org/10.1016/j.ndteint.2004.11.002.
[25] Mook G, Lange R, Koeser O. Non-destructive characterisation of carbon-fibre-reinforced plastics by means of eddy-currents. Compos Sci Technol 2001;61:865–73. https://doi.org/10.1016/S0266-3538(00)00164-0.
[26] De Goeje MP, Wapenaar KED. Non-destructive inspection of carbon fibre-reinforced plastics using eddy current methods. Composites 1992;23:147–

57. https://doi.org/10.1016/0010-4361(92)90435-W.
[27] Koyama K, Hoshikawa H, Kojima G. Eddy current nondestructive testing for carbon fiber-reinforced composites. J Press Vessel Technol Trans ASME 2013;135:1–2. https://doi.org/10.1115/1.4023253.
[28] He Y, Tian G, Pan M, Chen D. Impact evaluation in carbon fiber reinforced plastic (CFRP) laminates using eddy current pulsed thermography. Compos Struct 2014;109:1–7. https://doi.org/10.1016/j.compstruct.2013.10.049.
[29] Heuer H, Schulze M, Pooch M, Gäbler S, Nocke A, Bardl G, et al. Review on quality assurance along the CFRP value chain - Non-destructive testing of fabrics, preforms and CFRP by HF radio wave techniques. Compos Part B Eng 2015;77:494–501. https://doi.org/10.1016/j.compositesb.2015.03.022.
[30] Fierro GPM, Flora F, Meo M. Thermal wave imaging for defect determination during automated fibre placement. Struct. Heal. Monit. 2019 Enabling Intell. Life-Cycle Heal. Manag. Ind. Internet Things - Proc. 12th Int. Work. Struct. Heal. Monit., vol. 2, DEStech Publications Inc.; 2019, p. 2294–301. https://doi.org/10.12783/shm2019/32369.
[31] Flora F, Boccaccio M, Malfense Fierro GP, Meo M. Non-destructive thermography-based system for damage localisation and characterisation during induction welding of thermoplastic composites. Thermosense Therm. Infrared Appl. XLII, 2020, p. 19. https://doi.org/10.1117/12.2564925.
[32] Induction Welding. Handb. Plast. Join., Elsevier; 2009, p. 113–20. https://doi.org/10.1016/b978-0-8155-1581-4.50013-5.
[33] Ahmed TJ, Stavrov D, Bersee HEN, Beukers A. Induction welding of thermoplastic composites-an overview. Compos Part A Appl Sci Manuf 2006;37:1638–51. https://doi.org/10.1016/j.compositesa.2005.10.009.
[34] Rudolf R, Mitschang P, Neitzel M. Induction heating of continuous carbon-fibre-reinforced thermoplastics. Compos Part A Appl Sci Manuf 2000;31:1191–202. https://doi.org/10.1016/S1359-835X(00)00094-4.
[35] Farahani RD, Dub M. Novel Heating Elements for Induction Welding of Carbon Fiber / Polyphenylene Sulfide Thermoplastic Composites 2017;1700294:1–10. https://doi.org/10.1002/adem.201700294.
[36] Rudnev V, Loveless D, Cook raymond L. Handbook of Induction Heating. 2002. https://doi.org/10.1201/9781420028904.
[37] He Y, Chen S, Zhou D, Huang S, Wang P. Shared excitation based nonlinear ultrasound and vibrothermography testing for CFRP barely visible impact damage inspection. IEEE Trans Ind Informatics 2018;14:5575–84. https://doi.org/10.1109/TII.2018.2820816.
[38] Netzelmann U, Walle G. Induction Thermography as a Tool for Reliable Detection of Surface Defects in Forged Components. n.d.
[39] Ibarra-Castanedo C, Piau J-M, Guilbert S, Avdelidis NP, Genest M, Bendada A, et al. Comparative Study of Active Thermography Techniques for the Nondestructive Evaluation of Honeycomb Structures. Res Nondestruct Eval 2009;20:1–31. https://doi.org/10.1080/09349840802366617.
[40] Carslaw H, Jaeger J. Conduction of heat in solids 1992.
[41] Zheng K, Chang YS, Wang KH, Yao Y. Improved non-destructive testing of carbon fiber reinforced polymer (CFRP) composites using pulsed thermograph. Polym Test 2015;46:26–32. https://doi.org/10.1016/j.polymertesting.2015.06.016.

[42] Wang Z, Tian GY, Meo M, Ciampa F. Image processing based quantitative damage evaluation in composites with long pulse thermography. NDT E Int 2018;99:93–104. https://doi.org/10.1016/j.ndteint.2018.07.004.
[43] Benítez H, Maldague X, Ibarra-Castanedo C, Loaiza H, Bendada A, Caicedo E. Modified differential absolute contrast using thermal quadrupoles for the nondestructive testing of finite thickness specimens by infrared thermography. Can. Conf. Electr. Comput. Eng., Institute of Electrical and Electronics Engineers Inc.; 2006, p. 1039–42. https://doi.org/10.1109/CCECE.2006.277741.
[44] Arndt RW. Square pulse thermography in frequency domain as adaptation of pulsed phase thermography for qualitative and quantitative applications in cultural heritage and civil engineering. Infrared Phys Technol 2010;53:246–53. https://doi.org/10.1016/j.infrared.2010.03.002.